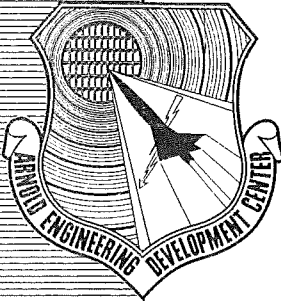


AEDC-TDR-62-202



PARTICLE-SOLID IMPACT PHENOMENA

By

C. D. Liles and E. H. Goodman
von Kármán Gas Dynamics Facility
ARO, Inc.

TECHNICAL DOCUMENTARY REPORT NO. AEDC-TDR-62-202

November 1962

AFSC Program Area 802A, Project 7342, Task 734202

PROPERTY OF U. S. AIR FORCE
AEDC LIBRARY
AF 40(600)1000

(Prepared under Contract No. AF 40(600)-1000 by ARO, Inc.,
contract operator of AEDC, Arnold Air Force Station, Tenn.)

AEDC TECHNICAL LIBRARY



ARNOLD ENGINEERING DEVELOPMENT CENTER
AIR FORCE SYSTEMS COMMAND
UNITED STATES AIR FORCE

NOTICES

Qualified requesters may obtain copies of this report from ASTIA. Orders will be expedited if placed through the librarian or other staff member designated to request and receive documents from ASTIA.

When Government drawings, specifications or other data are used for any purpose other than in connection with a definitely related Government procurement operation, the United States Government thereby incurs no responsibility nor any obligation whatsoever; and the fact that the Government may have formulated, furnished, or in any way supplied the said drawings, specifications, or other data, is not to be regarded by implication or otherwise as in any manner licensing the holder or any other person or corporation, or conveying any rights or permission to manufacture, use, or sell any patented invention that may in any way be related thereto.

PARTICLE-SOLID IMPACT PHENOMENA

By

C. D. Liles and E. H. Goodman
von Kármán Gas Dynamics Facility
ARO, Inc.
a subsidiary of Sverdrup and Parcel, Inc.

November 1962

ARO Project No. 381146

1

2

3

4

5

6

7

8

9

10

11

12

13

14

15

16

17

18

19

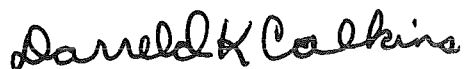
20

ABSTRACT

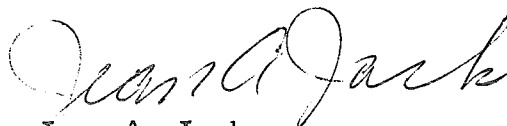
High velocity impact tests have been made with high purity aluminum and copper projectiles and targets. Data are presented for impact velocities from 0.762 to 7.62 km/sec, and these are compared with various correlation formulas.

PUBLICATION REVIEW

This report has been reviewed and publication is approved.



Darreld K. Calkins
Major, USAF
AF Representative, VKF
DCS/Test



Jean A. Jack
Colonel, USAF
DCS/Test

17

18

19

20

21

22

23

24

25

26

27

28

29

30

31

32

33

CONTENTS

	<u>Page</u>
ABSTRACT.	iii
NOMENCLATURE.	vii
1.0 INTRODUCTION	1
2.0 APPARATUS	
2.1 Launcher and Range.	1
2.2 Projectiles and Targets	2
2.3 Instrumentation.	2
3.0 PROCEDURE	
3.1 Test Procedure.	3
3.2 Data Reduction Procedure	3
3.2.1 Velocity Data Reduction.	3
3.2.2 Impact Crater Data Reduction	3
3.2.3 Accuracy of Velocity Measurements	4
3.2.4 Accuracy of Crater Measurements	4
4.0 RESULTS AND DISCUSSION	
4.1 Penetration Data	5
4.2 Crater Shape	7
4.3 Crater Volume	7
5.0 CONCLUSIONS	8
REFERENCES	8

TABLES

1. Physical Properties of Target Materials.	11
2. Variation in Size and Weight of Spherical Projectiles	11
3. Tabulated Velocity and Crater Data	12

ILLUSTRATIONS

Figure

1. Typical Hyperballistic Impact Range Layout.	15
2. Typical Target Hardness Distribution on Copper Target	16
3. Schematic of Framing Camera and Optical Components	17

<u>Figure</u>	<u>Page</u>
4. Photograph of Projectile and Sabot.	18
5. Photograph of Sabot Stripper	19
6. Four Frames from a Typical Framing Camera Sequence Showing Projectile and Target	20
7. Variation of Maximum Possible Error in Framing Camera Turbine Speed.	21
8. Penetration Data	22
9. Correlation of Data with Theoretical and Empirical Penetration Prediction Equations	24
10. Crater Depth to Diameter Ratio for Copper and Aluminum Spheres into Copper and Aluminum Targets.	26
11. Correlation of Crater Volume Data with Empirical Volume Prediction Equations	27

NOMENCLATURE

Al \rightarrow Cu	Aluminum projectile impacted on a copper target
c	Sonic velocity in target material
D _c	Diameter of crater
d	Diameter of spherical projectile
H	Brinell hardness number of the target
m _p	Mass of projectile
P	Penetration, depth of crater
u _p	Projectile velocity
V _c	Crater volume
V _p	Projectile volume
ρ_p	Projectile density
ρ_t	Target density

10

11

12

13

14

15

16

17

18

19

20

21

22

23

24

25

26

27

28

29

30

31

32

33

34

35

36

1.0 INTRODUCTION

Tests were conducted in the von Kármán Gas Dynamics Facility (VKF), Arnold Engineering Development Center (AEDC), Air Force Systems Command (AFSC), USAF, for the Aeronautical Systems Division (ASD), AFSC, to provide experimental data on the phenomena which occur during hypervelocity impact of solid particles against solids. This project has been coordinated with the Plastics Section, National Bureau of Standards (NBS), where additional analysis of the data will be performed.

The tests required impacts of 1/16-, 1/8-, and 3/16-in. -diam aluminum and copper spherical projectiles on targets of like and unlike material at velocities from 0.6 to 7.6 km/sec. The experimental data required were impact crater volume, diameter, and depth measurements.

Tests were conducted in the Hyperballistic Impact Range (S-1) from July 10, 1961, until June 25, 1962.

2.0 APPARATUS

2.1 LAUNCHER AND RANGE

The Hyperballistic Impact Range S-1 consists of: (1) a two-stage launcher, (2) an expansion tank to absorb muzzle blast and to provide space for separation of the projectile from the sabot, (3) a connecting tube which has provision for measuring projectile velocity, and (4) a target chamber. These are shown in the sketch of a typical hyperballistic range (Fig. 1). The overall length of the S-1 range is approximately 80 ft, and the projectile travel from the launch tube muzzle to the target is approximately 55 ft. A detailed description of the range is given in Ref. 1.

The launcher is a powder-driven, two-stage, light-gas launcher. The launch tubes presently used are 7.6 mm, 200 calibers long. Reference 2 describes the launcher and launcher performance in detail.

2.2 PROJECTILES AND TARGETS

The projectiles and targets were supplied by the National Bureau of Standards. The projectile and target materials are pure (99.99 percent) aluminum and oxygen-free, high-conductivity (99.96 percent) copper. Both projectiles and targets were annealed to reduce the effects of work hardening. Table 1 shows the physical properties of the aluminum and copper target materials. The physical properties of the projectiles are assumed to be the same as those for the targets of like material because the projectiles were annealed under the same conditions as the targets. Figure 2 shows the hardness distribution of a typical copper target; the hardness distribution for the aluminum targets is similar. The Brinell hardness distribution between targets was 48.9 to 50.9 for the copper targets and 15.9 to 17.8 for the aluminum. The variation in size and weight of the spherical projectiles is shown in Table 2.

2.3 INSTRUMENTATION

The velocity measurements were made with the Beckman & Whitley (B&W) Model 192 framing camera. This camera has a maximum framing rate of 1.4×10^6 frames/sec. A sketch of the B&W setup is shown in Fig. 3. The light output from the xenon tube backlights a translucent, plastic screen against which the projectile and target face are silhouetted. The light duration can be adjusted between 30 to 300 μ sec, allowing proper exposure of 82 frames on the B&W film without rewrite or the use of a blast shutter. The 7-in. -diam field of view of the B&W camera allows both impact and pre-impact events to be recorded.

The B&W light source trigger, shown in Fig. 3, is a capacitance-type trigger which consists of two sheets of aluminum film separated by a sheet of Mylar film. The total thickness of the trigger is approximately 0.0127 mm. With a potential across the two sides of the aluminum-Mylar film, triggering occurs when the projectile punctures the film and completes the circuit. Since this triggering method requires physical contact with the projectile, a magnetic coil trigger is under development which makes no such requirement. Three shots were made using the magnetic coil to determine the effect of the aluminum-Mylar trigger on the crater data. The effect is discussed in section 4.1 of this report.

3.0 PROCEDURE

3.1 TEST PROCEDURE

The projectile was seated in a sabot (Fig. 4) and then inserted into the launch tube. The sabot carries the projectile through the bore, prevents it from losing material by friction, protects it from the hot propellant, and forms a seal to prevent blow-by.

At the beginning of the test, no attempt was made to prevent the sabot from impacting on the target. Because the projectile craters were too close to the impacts of the sabot, only four good data shots in ten were obtained. A mechanical sabot-stripping device (Fig. 5) was subsequently developed which stripped the sabot from the projectile as it emerged from the muzzle of the launch tube, allowing the projectile to impact at a point far enough from craters formed by the sabot fragments to avoid interference by them. This sabot stripper consists of four rods or wires that intercept the sabot at the muzzle, retarding it and causing its course to diverge from the projectile's. Use of this device resulted in approximately seven good data shots in ten.

3.2 DATA REDUCTION PROCEDURE

3.2.1 Velocity Data Reduction

The projectile velocity and condition just prior to its arrival at the target were recorded on the B&W film. Accurately printed lines on the translucent screen, against which the projectile is silhouetted, allowed the projectile's position to be computed and the velocity at impact determined by a least squares fit in a computer program. Figure 6 is typical of a series of frames showing the projectile and target.

3.2.2 Impact Crater Data Reduction

Crater volume, which is defined as the volume below the original target surface, was determined by accurately metering a solution into the crater. To eliminate the error in solution level due to meniscus, a one-percent Alconox-water solution was used. A detailed description of this procedure is given in Ref. 1.

The crater diameter was measured by traversing the vernier table of an optical comparator until the cross-hair of a cathetometer was tangent to the opposite side of the crater at the solution contact level. Hence, the distance through which the vernier table traveled was the

crater diameter at that solution level. The target was then rotated approximately 90 deg, and the measurement was made again. The average of several readings was the reported crater diameter. Crater depth was determined using an optical depth micrometer.

3.2.3 Accuracy of Velocity Measurements

The error in distance measurements is due to the inability to read the exact position of the projectile on the frame of the film and poor resolution of the projectile image. The standard error for position, using a Gaussian least squares curve fit, is within 0.25 percent of the base distance. When this error was larger, more points were read from the film. The random deviations were the same for all film reading devices used.

The error in time stems directly from the error in the camera turbine speed as shown by the equation:

$$\text{camera framing rate} = 240 \times \text{turbine speed (frames/sec)} \quad (1)$$

where turbine speed is in revolutions per second. The error in time is divided further into two parts: (1) error due to turbine drift and (2) counter error.

For turbine speeds below 2500 rps there is no appreciable drift in turbine speed; however, as the turbine speed increases above 2500 rps, the drift increases appreciably. An average drift in a 1-sec counting period of ± 10 revolutions at a turbine speed of 5000 rps has been observed for approximately 30 shots. The only significant counter error is a possible ± 1 revolution during each counting period.

Figure 7 shows the maximum error in turbine speed and, therefore, in the time base for the range of turbine speeds and the counting periods used during the test. Seventy data shots were made using the 1-sec counting period and turbine speeds from 1000 to 5300 rps, and 53 data shots were made using the 0.1-sec counting period and turbine speeds from 4500 to 5500 rps.

The errors in time and distance allow an absolute velocity determination within one percent.

3.2.4 Accuracy of Crater Measurements

To determine the accuracy of the crater measuring technique, two hemispherical craters were machined in a metal target. The calculated volume of the craters was compared with the volume derived by metering

an Alconox-water solution and the volume determined by the weight of the metered solution. The solution was metered from a hypodermic syringe, pipettes, and burettes. Volumes measured with each of the fluid metering devices were repeatable to ± 0.3 percent. The difference between the calculated volumes and the measured volumes was less than one percent.

The depth, as determined by the optical depth micrometer, was repeatable to within ± 0.005 mm. The diameter measurement was repeatable to ± 0.127 mm for three measurements.

The evaporation rate of the one-percent Alconox-water solution is one percent per hour as determined from a 2.32-cm^2 surface area at 25.5°C and 736 mm Hg. Since all of the measurements are made within five minutes, the error attributed to evaporation is considered to be negligible.

4.0 RESULTS AND DISCUSSION

Tabulation of velocity and crater dimensions is given in Table 3. The data are grouped by projectile and target combinations and by projectile size.

4.1 PENETRATION DATA

The raw penetration data, as presented in Fig. 8, have been reduced to the dimensionless form, P/d versus u_p/c , where penetration, P , is the distance from the original target surface to the bottom of the crater; i. e., in some cases there is a thin layer of projectile material plated on the wall and bottom of the crater (Al \rightarrow Al, Al \rightarrow Cu, and Cu \rightarrow Cu). This thickness has not been accounted for in the penetration measurement. The Cu \rightarrow Al series produced different craters. One projectile remained intact after impact but later fell out for the Cu \rightarrow Al (0.772 km/sec), but on all other Cu \rightarrow Al impacts the copper projectile disintegrated, leaving small, embedded globules in the wall and bottom of the crater.

If the aluminized Mylar sheet, which was used for a projectile detector device (discussed in section 2.3), has any effect on crater formation, it can not be distinguished from the experimental scatter of the normal data. This is shown in Fig. 8. The flagged data were obtained with the use of a magnetic detector. The other data were obtained with the use of the aluminized Mylar as the projectile detector.

The penetration data were correlated with the empirical relationship based upon the kinetic energy of the projectile and the resistance of target material

$$(\rho_t c^2 / 2) (2/3 \pi P^3) = K (\rho_p / \rho_t) (m_p u_p / 2)^2$$

or

$$P/d = K_1 (\rho_p / \rho_t)^n (u/c)^{2/3} \quad (2)$$

where $2/3 \pi P^3$ is the crater volume, P is the penetration, and $n = 2/3$, which was first used by Charters (Ref. 3) with the values, $n = 0.69$ and $K_1 = 2.28$, and later modified by Summers (Ref. 4) where $n = 2/3$ and $K_1 = 2.28$. By plotting P/d at $u/c = 1$ versus ρ_p / ρ_t for the four projectile-target combinations, the exponent of the density ratio term may be obtained. The constant K_1 is then obtained by fitting a straight line to the log of the penetration and the log of density ratio times the log of the impact Mach number. The correlation of the present data results in the relationship

$$P/d = 2.35 (\rho_p / \rho_t)^{0.70} (u_p/c)^{2/3} \quad (3)$$

which is shown in Fig. 9. The value of $K_1 = 2.35$ was determined by averaging over the complete body of data, thereby giving data from each projectile-target system equal weight. The K_1 values for each projectile-target system are 2.10, 2.57, 2.32, and 2.41 for the Cu→Cu, Cu→Al, Al→Cu, and Al→Al, respectively.

A least squares fit whereby both the constant and the velocity exponent were correlated with the experimental values is also shown in Fig. 9. This was computed from

$$\log y = n \log x + \log b \quad \text{or} \quad y = b x^n$$

where $\log(K_1) = \log(P/d) - 0.7 \log(\rho_p / \rho_t) - n \log(u_p/c)$. These values for the target-projectile systems for the K_1 constant and velocity exponent, n , are $K_1 = 2.05$ $n = 0.90$, $K_1 = 2.60$ $n = 0.63$, $K_1 = 2.14$ $n = 0.79$, $K_1 = 2.37$ $n = 0.57$ for the Cu→Cu, Cu→Al, Al→Cu, and Al→Al, respectively.

Correlation with other empirical expressions involving projectile momentum, target hardness, and velocity of sound of the projectile material were also attempted but were found to be insufficient for predicting the effects of hypervelocity impact. These expressions are derived and discussed in Ref. 5.

Several theoretical analyses are presently available. In general, they may be divided into four groups: (1) Rigid Projectile, (2) Hydrodynamic, (3) Thermal Penetration, and (4) Explosive Analogy. The

experimental data and pertinent theories of each group were compared. Unfortunately, most of the theories apply to thin plates, but several have been extended to cover special cases for thicker targets. Adequate correlations could not be attained with most of these theories. A theoretical formula was derived by Bohn and Fuchs (Ref. 6) based on low velocity penetration considerations but considered by them to be applicable to meteoroid impact. The formula is the following:

$$P/d = (1/2 \rho_p/\rho_t)^n \left\{ \ln \left[1 + (B/3)^{1/2} \right] - \frac{(B/3)^{1/2}}{1 + (B/3)^{1/2}} \right\} \quad (4)$$

where

$$B = \frac{\rho_t + u_p^2}{H} \quad (\text{Ref. 4, Best})$$

and

$$n = 1$$

It was found that if n is taken as $2/3$ as in Ref. 4, a reasonably good fit to the four target-projectile combinations is obtained (Fig. 9).

4.2 CRATER SHAPE

Several of the empirical expressions and theoretical analyses (Ref. 5) use the simplifying assumption that the crater is hemispherical ($P/D_c = 0.5$). Figure 10 shows the parameter, P/D_c , versus projectile velocity. The Al→Cu craters appear to approach a hemispherical form with increasing velocity. The similar projectile-target combinations have a limit of about 0.55. Within the range of velocities obtained, craters in aluminum by copper projectiles were deeper ($P/D_1 > 0.8$) than hemispherical, although the tendency is still in that direction. The data suggest that at very high velocity, the form of craters will be deeper than hemispherical.

4.3 CRATER VOLUME

Crater volume data are shown in Fig. 11 in the dimensionless form, V_c/V_p versus u_p/c . Correlation of the data with equation

$$V_c/V_p = K_2 (\rho_p/\rho_t)^{3/2} (u_p/c)^2 \quad (5)$$

is also shown. The constant, K_2 , and the density ratio exponent were derived from the experimental data using the same method as described in section 4.2. The crater volume equation (Eq. 5) and the penetration equation (Eq. 3) are not compatible with the assumption of hemispherical

craters. A less accurate correlation is obtained by using the equation

$$V_c/V_p = K (\rho_p/\rho_t)^2 (u_p/c)^2 \quad (6)$$

which is compatible with the hemispherical assumption (the cube of Eq. (2) for $n = 2/3$).

The value of $K_2 = 44.1$ is the average value of the projectile-target systems. Values for each system are 35.9, 46.2, 41.0, and 53.4 for Cu→Cu, Cu→Al, Al→Cu, and Al→Al, respectively.

Figure 11 also shows the best least squares fit. The velocity exponents K_2 and (n) are $K_2 = 35.7$ $n = 1.79$, $K_2 = 46.2$ $n = 2.02$, $K_2 = 45.7$ $n = 1.48$, and $K_2 = 50.6$ $n = 1.68$, for Cu→Cu, Cu→Al, Al→Cu, and Al→Al, respectively.

5.0 CONCLUSIONS

When the experimental data are correlated to the kinetic energy of the projectile, the following empirical relations are adequate for engineering purposes:

$$P/d = 2.35 (\rho_p/\rho_t)^{0.70} (u_p/c)^{2/3}$$

$$V_c/V_p = 44.10 (\rho_p/\rho_t)^{3/2} (u_p/c)^2$$

Penetration may be adequately described by Bohn and Fuch's theoretical analysis if the density term is modified.

The penetration to crater diameter ratios obtained at maximum attainable velocity were: Al→Cu about 0.45, Cu→Cu and Al→Al about 0.55, and Cu→Al about 0.8, which shows that the majority are nearly hemispherical; however, computations of crater volume which assume hemispherical shape can be significantly in error if a crater shape factor is not employed.

REFERENCES

1. Goodman, E. H. "Description of Terminal Ballistics Ranges." AEDC-TDR-62-104, May 1962.
2. Stephenson, W. B. "Performance of a Small Two-Stage Light-Gas Gun Used for Impact Testing." AEDC-TN-61-166, January 1962.

3. Charters, A. C. and Locke, G. S., Jr. "A Preliminary Investigation of High Speed Impact: The Penetration of Small Spheres into Thick Copper Targets." NACA RM-A58B26, May 1958.
4. Summers, J. L. "Investigation of High Speed Impact: Regions of Impact and Impact at Oblique Angles." NASA TN-D-94, October 1959.
5. Herrman, Walter and Jones, A. H. "Survey of Hypervelocity Impact Information." ASRL Report No. R-99-1, AD-267-290, October 1961.
6. Bohn, J. L. and Fuchs, O. P. "High Velocity Impact Studies Directed Toward the Determination of Spatial Density, Mass, and Velocity of Micrometeorites at High Altitudes." Temple University Scientific Report No. 1, January 1958.

TABLE 1
PHYSICAL PROPERTIES OF TARGET MATERIALS

Target Material	Brinell Hardness kg/mm ²	Approximate Variation in Hardness of Each Target kg/mm ²	Density gm/cm ³	Sonic Speed in Material* km/sec	Static Yield Strength** kg/mm ²	Ultimate Strength** kg/mm ²	Elongation** %	Reduction of Area** %
Copper	48.9-50.9	0.6	8.77	3.556	9.922	22.026	57.80	83.05
Aluminum	15.9-17.8	0.6	2.67	5.102	0.774	5.528	51.65	95.00

*Handbook values

**ASTM STANDARD 505 Tensile Test

TABLE 2
VARIATION IN SIZE AND WEIGHT OF SPHERICAL PROJECTILES

Size and Material	Average Diameter in.	Average Weight gm	Variation from Average Diameter %	Variation from Average Weight %
1/16" - Al (Group I)	0.0604	0.00519	---	0.42
1/8" - Al (Group I)	0.1260	0.04636	---	0.54
1/16" - Cu (Groups I & II)	0.0614	0.01778	0.14	0.056
1/8" - Cu (Group I)	0.1240	0.14535	---	0.90
1/16" - Al (Group II)	0.0620	0.00560	0.24	0.30
1/8" - Al (Group II)	0.1258	0.04660	0.16	0.32
1/8" - Cu (Group II)	0.1260	0.15460	0.12	0.07
3/16" - Al (Group III)	0.1877	0.15440	0.11	0.016
3/16" - Cu (Group III)	0.1874	0.50620	0.076	0.21

TABLE 3
TABULATED VELOCITY AND CRATER DATA

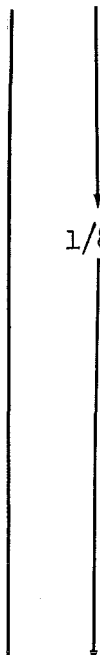


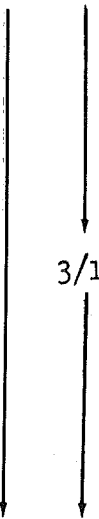

<u>Proj Mat/ Target Mat - Proj Diam</u>	<u>Shot No.</u>	<u>Velocity m/sec</u>	<u>Crater Depth mm</u>	<u>Crater Diam mm</u>	<u>Crater Volume ccx10⁻²</u>
<div style="display: flex; align-items: center; justify-content: center;"> <div style="text-align: center; margin-right: 10px;"> Al/Al-1/16"  </div> <div style="text-align: center; margin-right: 10px;"> 1/8"  </div> <div style="text-align: center;"> 3/16"  </div> </div>	W-47	3,200	2.446	5.715	5.326
	W-49	4,076	3.101	5.791	7.374
	W-51	5,322	3.536	7.061	9.124
	W-84	6,654	3.917	8.407	14.160
	W-89	6,793	3.980	8.611	14.160
	W-85	6,924	3.726	8.077	13.270
	W-86	7,292	4.249	8.738	15.490
	W-83	7,507	4.618	8.585	16.810
	W-18	2,048	3.990	9.246	13.440
	W-22	2,254	4.450	9.175	20.070
	W-20	2,263	4.448	9.480	20.660
	W-19	2,317	4.077	9.296	15.500
	W-14	2,348	4.691	8.313	15.980
	W-26	2,548	5.695	11.300	36.540
	W-42	4,549	7.295	14.860	77.500
	W-3	4,820	6.782	14.350	66.050
	W-41	5,148	7.584	15.160	86.850
	W-5	5,289	7.887	13.450	72.940
	W-8	5,612	8.291	16.320	107.350
	W-61	5,694	7.902	15.490	92.900
	W-67	5,751	7.366	15.240	81.900
	W-58	5,881	8.280	15.820	118.000
	W-65	6,920	9.360	18.300	143.000
	W-325	2,548	7.991	15.354	92.930
	W-190	2,977	8.951	17.107	131.300
	W-189	3,024	8.976	17.563	130.800
	W-191	3,049	9.050	17.158	135.200
	W-188	3,107	9.023	17.961	138.700
	W-194	3,131	9.258	17.145	140.600
	W-205	3,146	9.129	17.746	141.000
	W-195	3,447	9.512	18.660	158.300
	W-193	4,223	10.884	20.666	227.200
	W-192	4,727	11.941	22.730	286.700
	W-196	5,166	12.979	23.230	347.600
	W-197	5,404	12.957	23.602	358.900
	W-200	6,632	13.368	24.505	451.900
	W-199	6,884	13.632	26.251	467.100
	W-201	6,876	13.340	24.809	413.500
	W-202	6,925	13.917	26.124	478.900
	W-204	7,306	14.286	27.234	520.200

TABLE 3 (Continued)

<u>Proj Mat/ Target Mat - Proj Diam</u>	<u>Shot No.</u>	<u>Velocity m/sec</u>	<u>Crater Depth mm</u>	<u>Crater Diam mm</u>	<u>Volume ccx10⁻²</u>
<div style="text-align: center;">Al/Cu-1/16"</div> <div style="position: relative; height: 800px;"><div style="position: absolute; top: 25%; left: 50%; transform: translate(-50%, -50%);">1/8"</div><div style="position: absolute; bottom: 25%; left: 50%; transform: translate(-50%, -50%);">3/16"</div></div>	W-185	1,748	0.973	3.523	0.738
	W-332	3,134	1.239	4.227	1.475
	W-351	3,603	1.628	4.745	1.721
	W-334	5,106	2.141	5.517	3.442
	W-343	6,020	2.367	5.939	3.442
	W-339	6,106	2.286	5.619	3.934
	W-346	6,539	2.403	5.789	4.425
	W-340	7,205	2.540	6.254	4.589
	W-186	1,833	1.486	6.693	3.688
	W-187	2,324	1.986	7.284	7.376
	W-275	2,990	2.685	8.388	8.851
	W-263	4,357	3.955	10.193	17.700
	W-264	5,514	4.255	10.706	23.110
	W-266	6,141	4.608	11.539	26.060
	W-271	6,944	5.250	12.748	37.370
	W-274	6,400	4.780	11.944	30.980
	W-211	2,697	3.741	11.335	25.080
	W-326	2,973	3.835	12.268	29.010
	W-212	3,729	5.032	13.174	40.980
	W-213	3,914	5.283	13.090	43.760
	W-214	4,396	6.408	15.044	69.820
	W-218	4,645	5.743	14.315	57.530
	W-231	4,969	5.911	14.542	65.560
	W-232	5,309	6.617	15.727	80.870
	W-230	5,328	6.345	15.496	75.070
	W-219	5,377	6.091	15.292	68.350
	W-233	6,022	6.932	16.698	95.060
	W-215	6,106	6.815	16.665	88.010
	W-238	6,262	6.127	15.611	70.970
	W-239	6,563	7.224	17.260	103.090
	W-240	6,869	7.661	17.748	101.000
	W-237	6,896	7.836	18.026	121.900
	W-235	6,950	7.549	17.599	114.070
<div style="text-align: center;">Cu/Cu-1/16"</div> <div style="position: relative; height: 200px;"><div style="position: absolute; bottom: 25%; left: 50%; transform: translate(-50%, -50%);">1/8"</div></div>	W-11	806	6.096	2.372	0.623
	W-109	1,146	1.280	3.300	0.880
	W-12	1,289	1.087	2.430	0.820
	W-108	1,798	1.821	3.810	1.770
	W-54	5,038	4.247	7.788	14.340
	W-57	5,716	4.191	8.255	14.590
	W-81	6,775	4.844	8.966	20.800
	W-28	2,448	5.733	10.920	34.400
	W-29	3,287	6.881	12.620	53.670

TABLE 3 (Concluded)

Proj Mat/ Target Mat - Proj Diam	Shot No.	Velocity m/sec	Crater Depth mm	Crater Diam mm	Crater Volume ccx10 ⁻²
Cu/Cu-1/8" 	W-32	3,518	7.165	13.440	61.100
	W-33	3,582	6.708	13.340	57.200
	W-35	3,833	7.493	13.610	68.800
	W-37	3,978	7.577	13.970	72.270
	W-34	4,088	7.778	14.250	77.200
	W-7	4,908	8.428	15.390	107.400
	W-101	6,146	9.873	16.300	144.000
	W-98	6,305	9.835	17.650	157.000
	W-93	6,440	9.721	17.090	163.000
	W-206	2,926	9.959	17.220	160.800
	W-207	3,520	10.925	19.198	212.400
	W-243	4,038	11.844	21.573	270.100
	W-242	4,538	12.555	22.018	319.100
	W-207	4,605	12.916	22.528	333.000
	W-277	4,736	12.598	22.938	350.100
	W-300	5,270	13.909	23.546	416.100
	W-304	5,586	13.868	24.345	442.200
	W-307	5,967	13.945	25.370	482.200
Cu/Al-1/16" 	W-178	772	2.286	1.999	0.983
	W-179	1,313	3.797	3.383	2.950
	W-182	1,912	5.001	4.920	6.884
	W-183	2,276	5.461	5.454	10.330
	W-354	5,687	8.331	10.395	56.546
	W-250	6,090	9.169	11.221	60.970
	W-259	6,436	9.169	11.302	67.850
	W-169	1,278	8.331	6.916	27.040
	W-171	1,678	9.881	9.243	53.100
	W-173	2,133	3.797	11.601	100.300
	W-184	2,240	11.849	11.736	102.300
	W-283	3,604	14.757	16.556	256.000
	W-284	4,206	16.307	18.400	340.100
	W-294	5,340	18.974	21.170	485.100
	W-222	2,690	19.660	19.444	521.200
	W-228	3,086	20.472	21.544	636.300
	W-221	3,496	22.581	24.496	814.300
	W-229	3,741	22.758	25.749	904.200

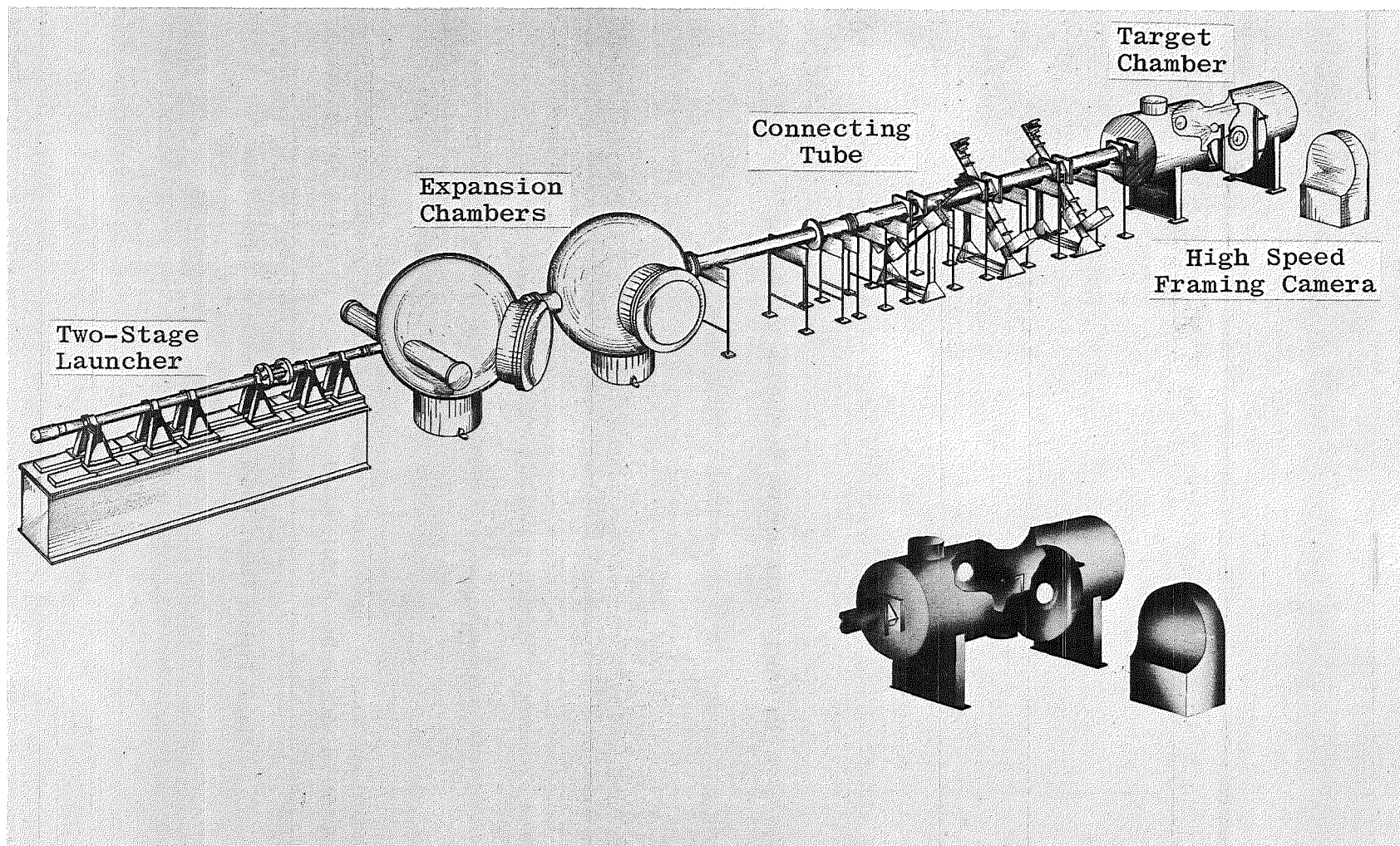


Fig. 1 Typical Hyperballistic Impact Range Layout

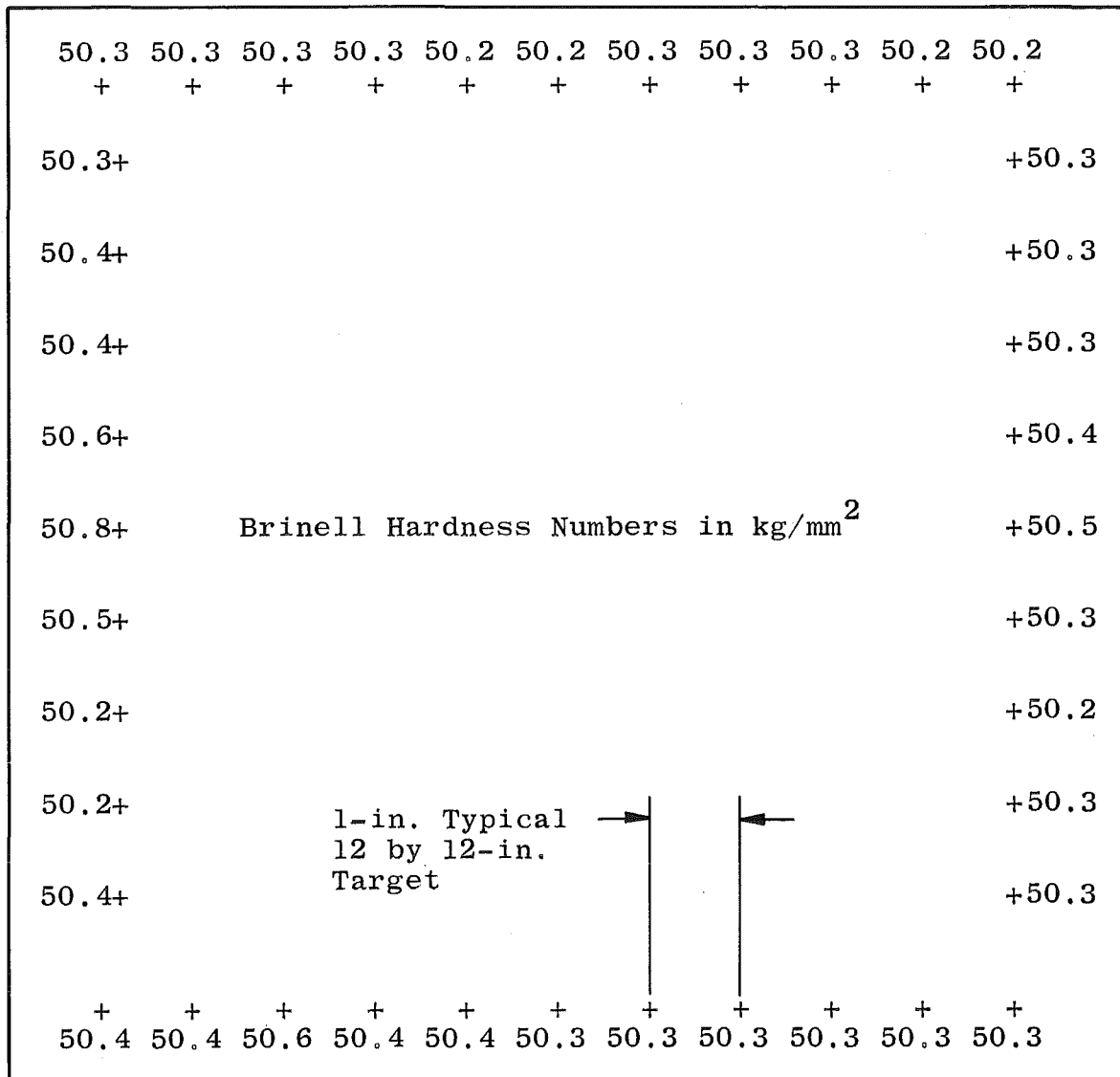


Fig. 2 Typical Target Hardness Distribution on Copper Target

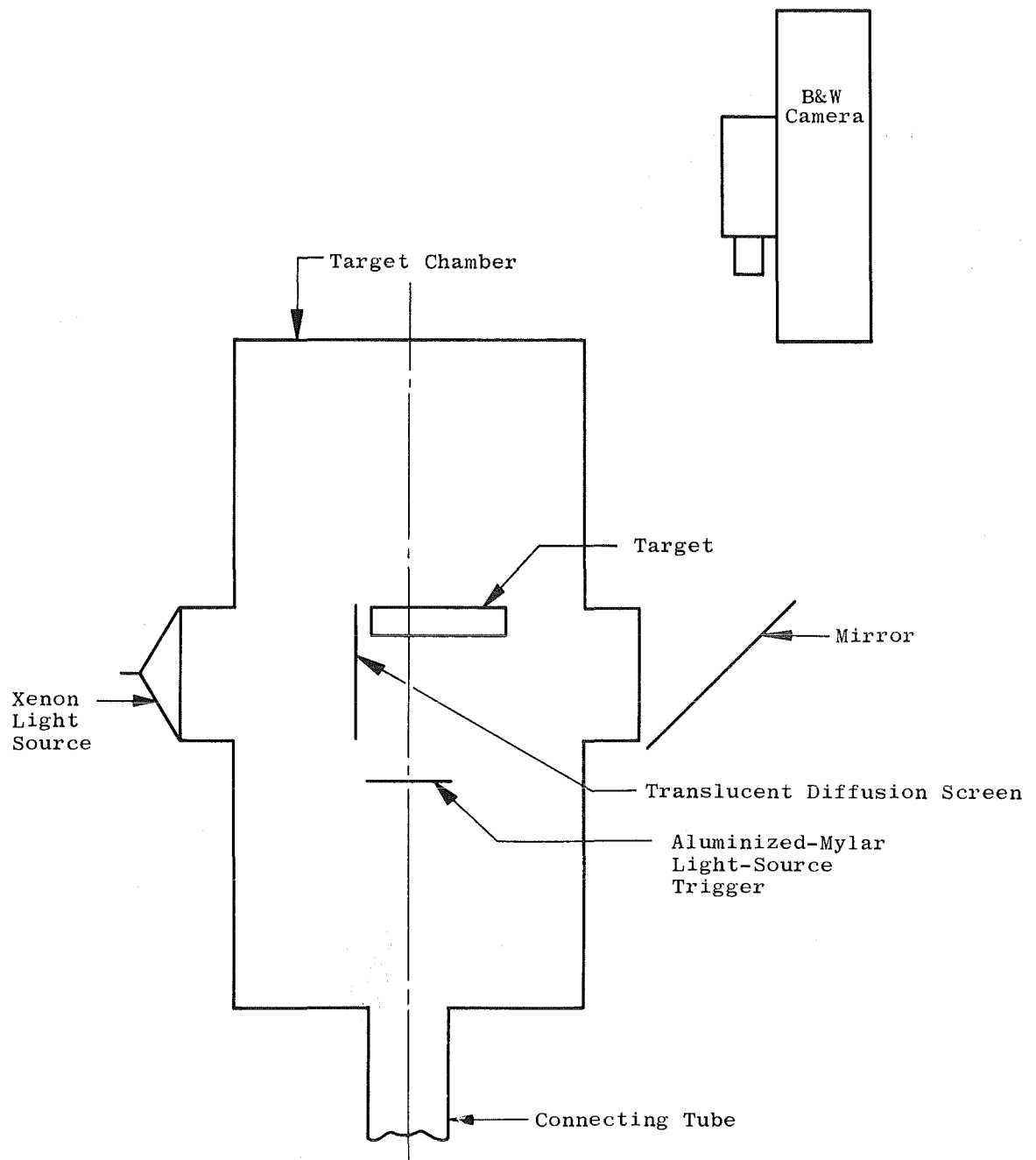


Fig. 3 Schematic of Framing Camera and Optical Components

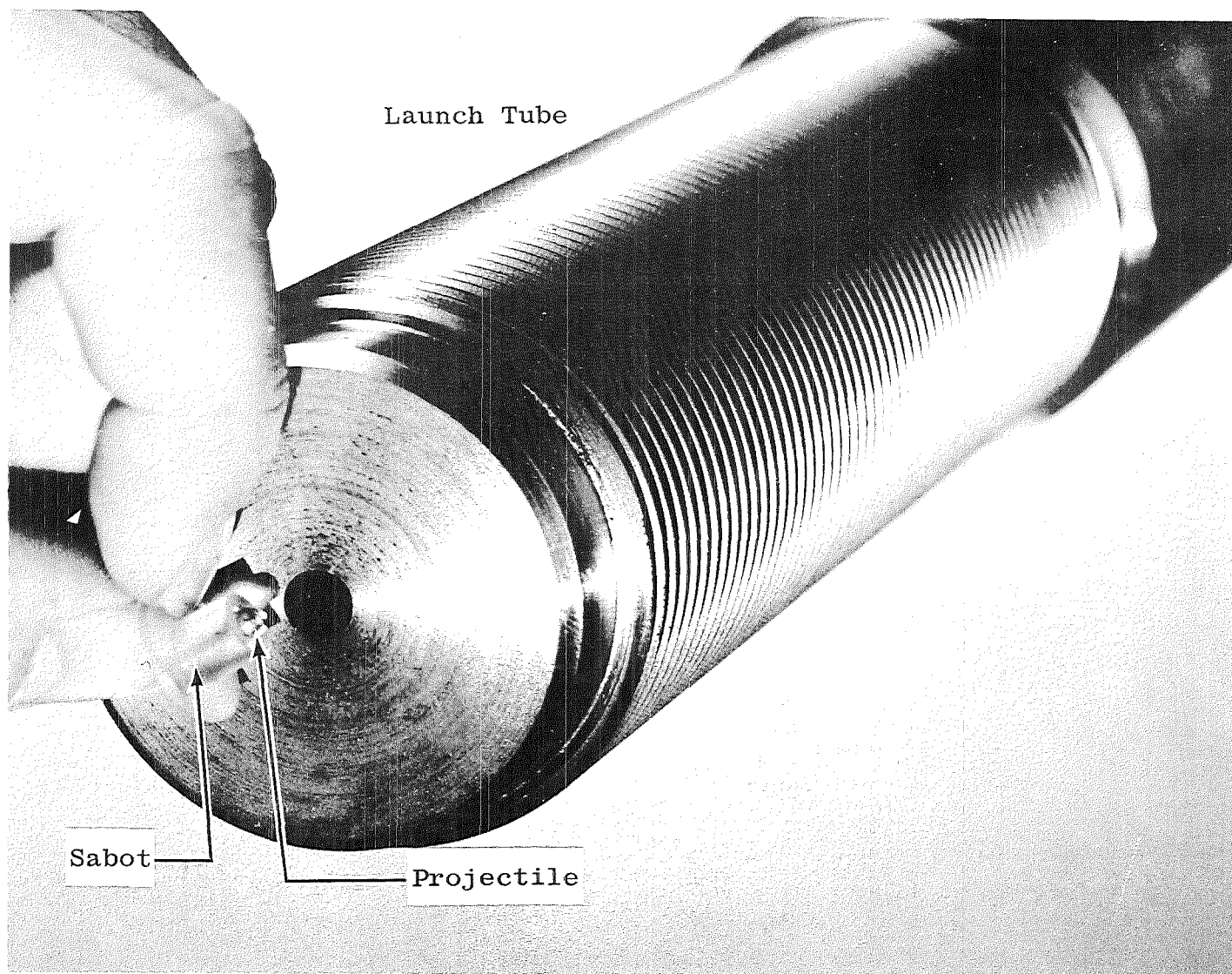


Fig. 4 Photograph of Projectile and Sabot

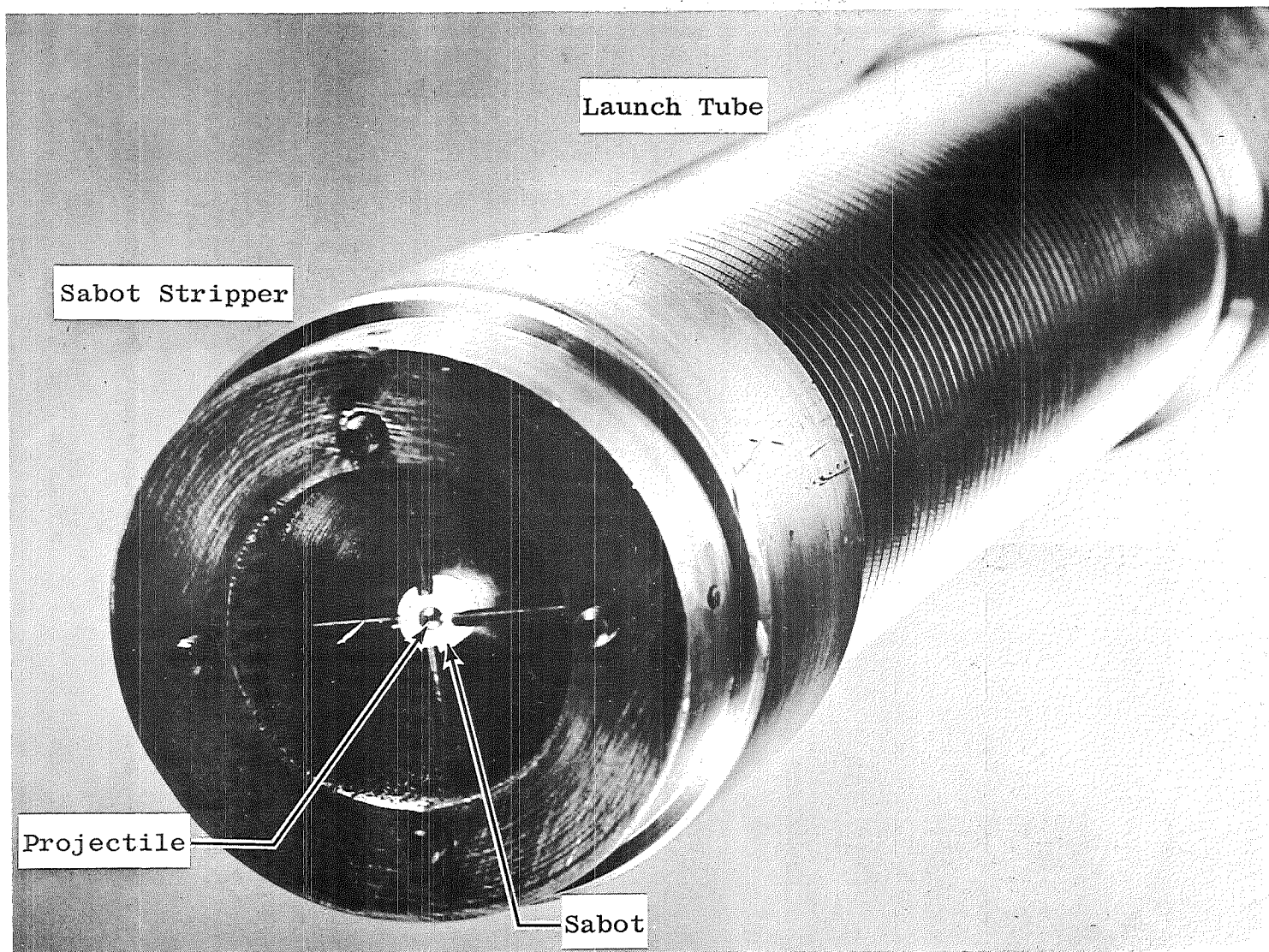
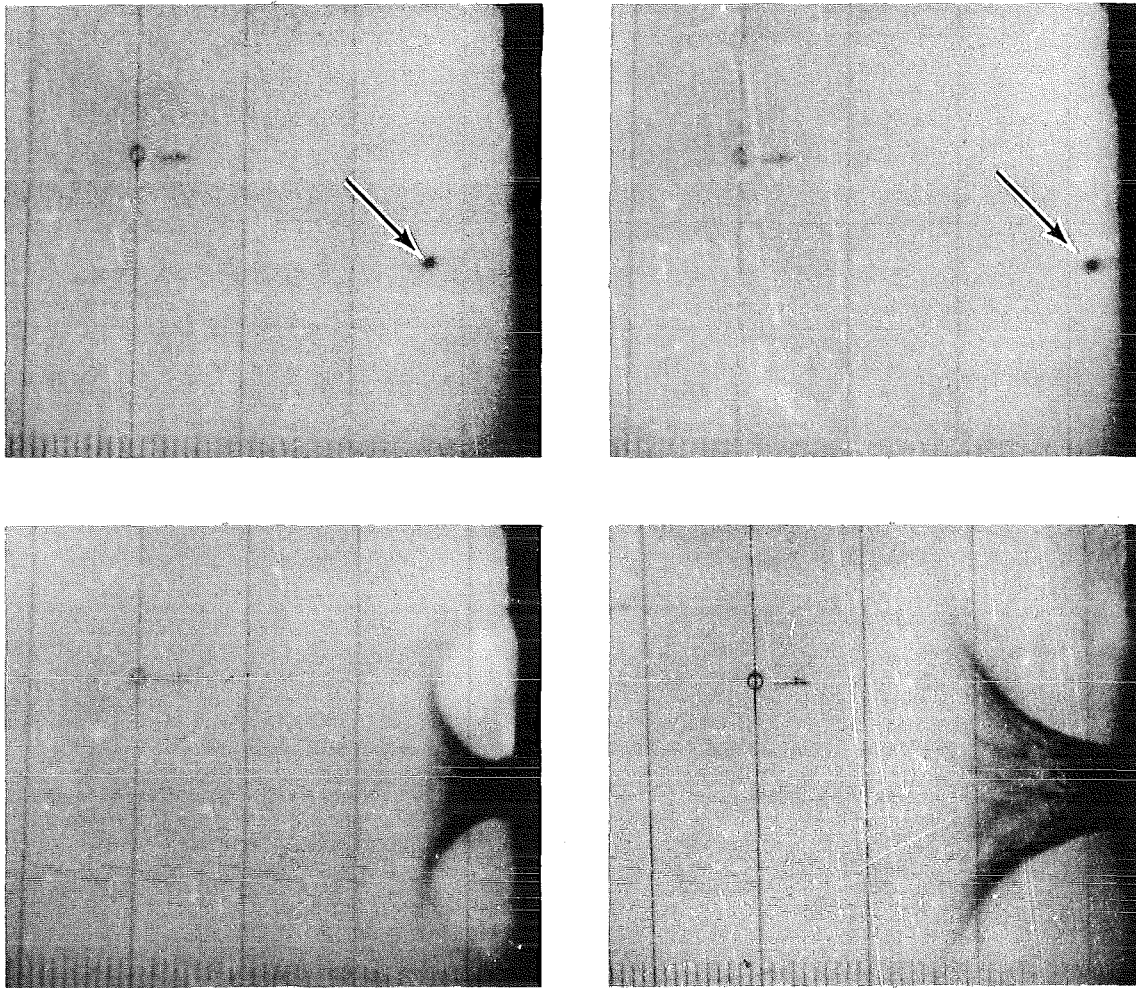


Fig. 5 Photograph of Sabot Stripper



Flight and Impact of a 1/8-in.-diam Aluminum Sphere
into an Aluminum Target at a Velocity of 6.523 km/sec

Fig. 6 Four Frames from a Typical Framing Camera Sequence Showing Projectile and Target

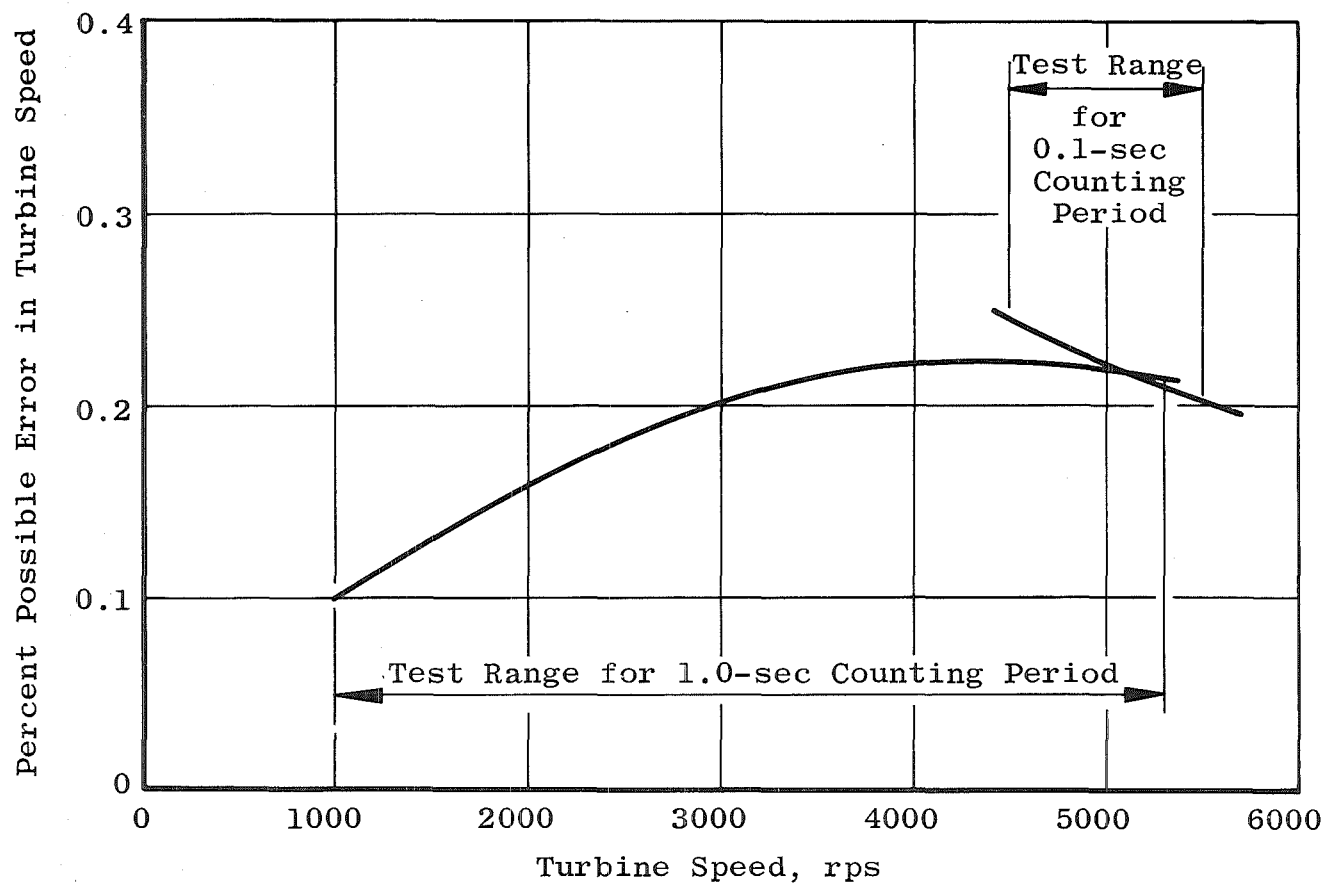


Fig. 7 Variation of Maximum Possible Error in Framing Camera Turbine Speed

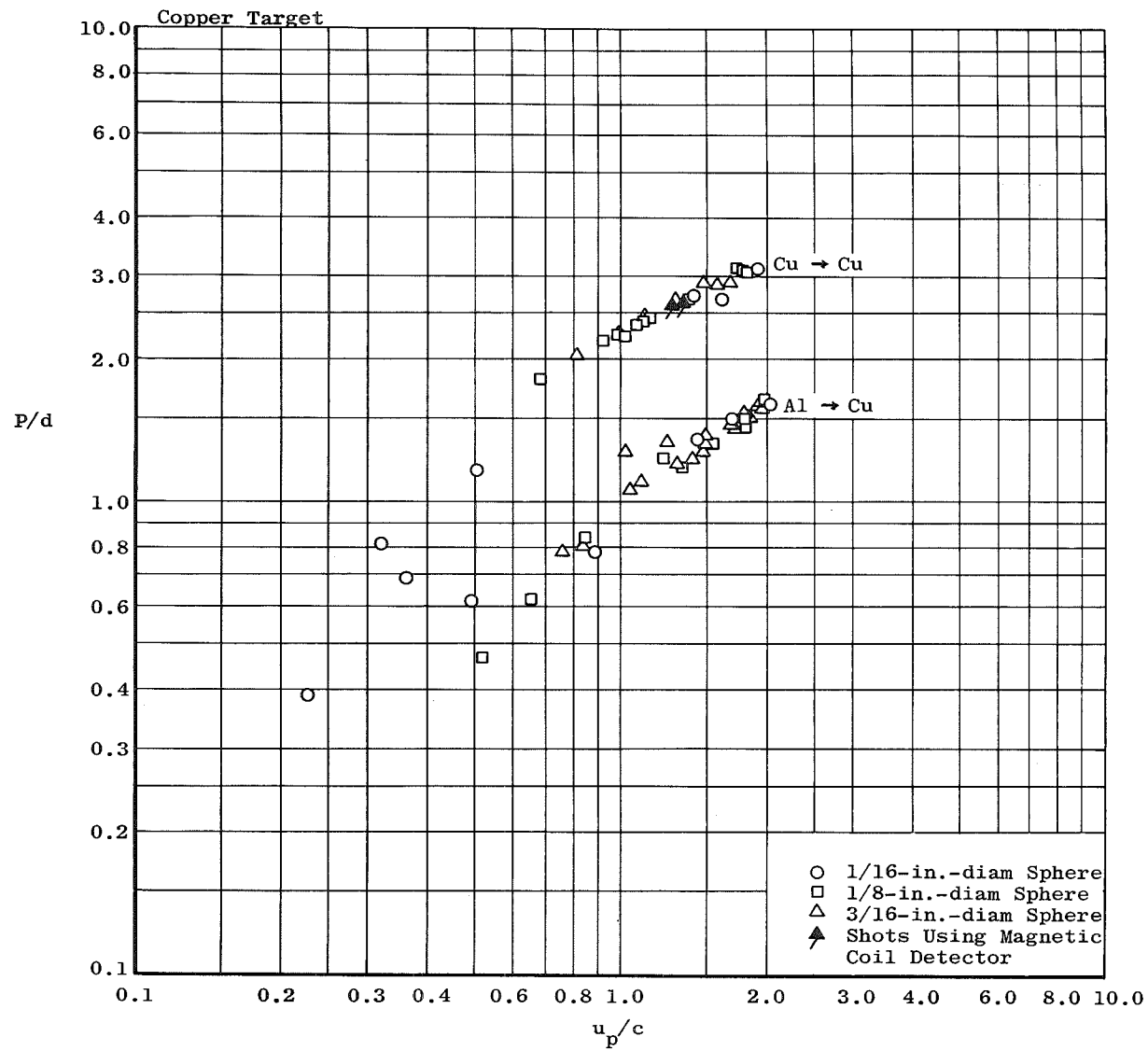


Fig. 8 Penetration Data

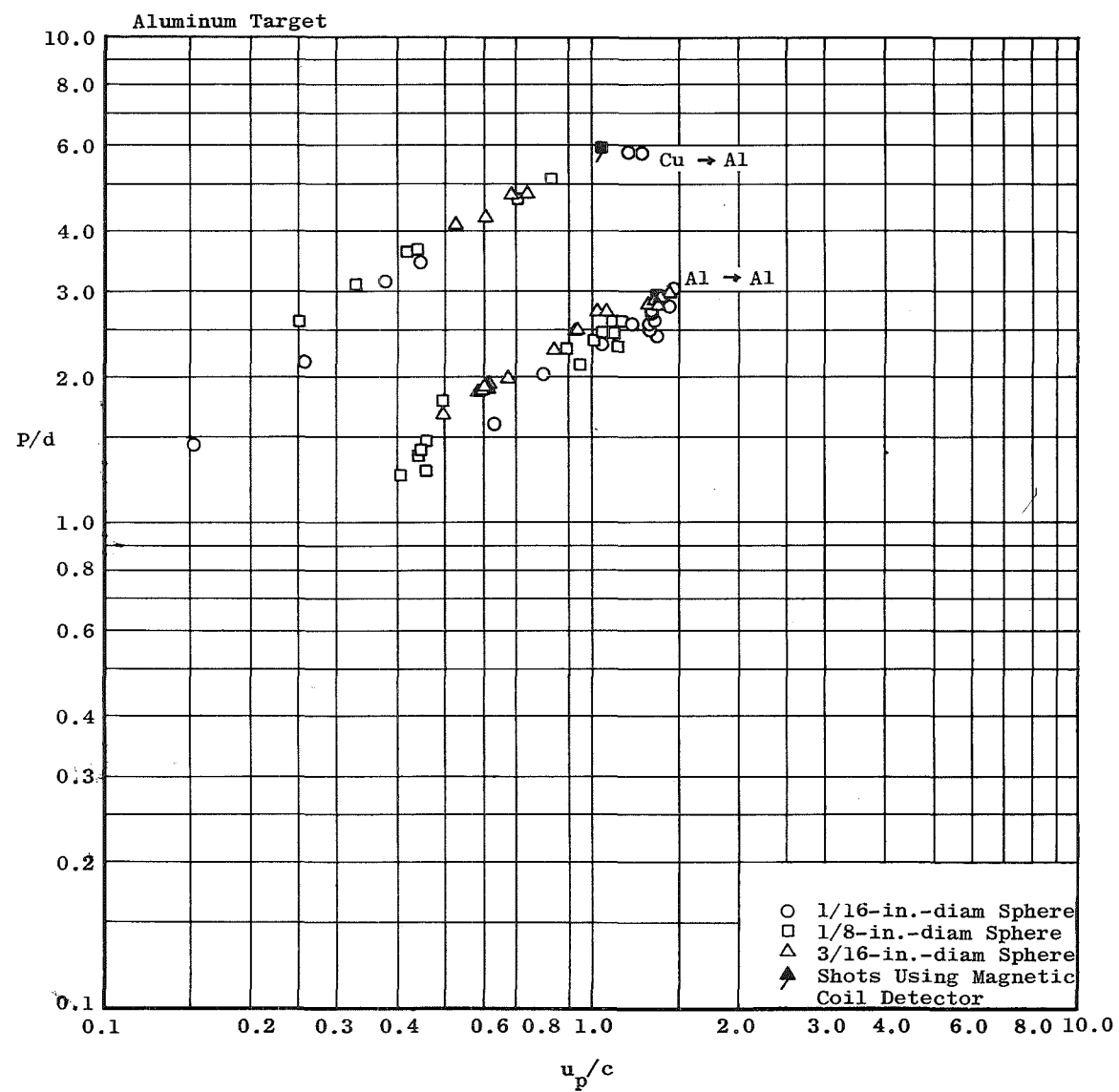


Fig. 8 Concluded

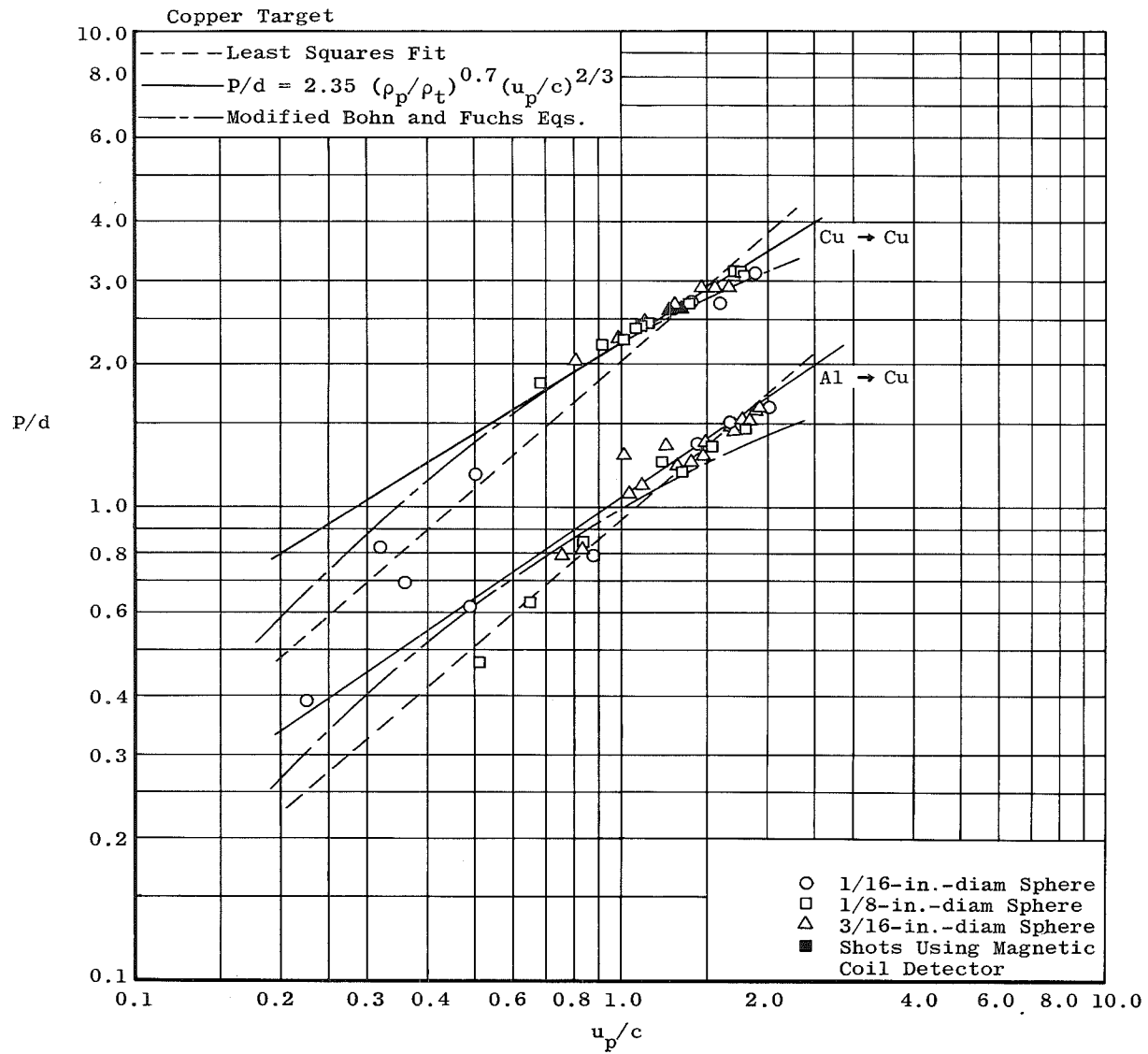


Fig. 9 Correlation of Data with Theoretical and Empirical Penetration Prediction Equations

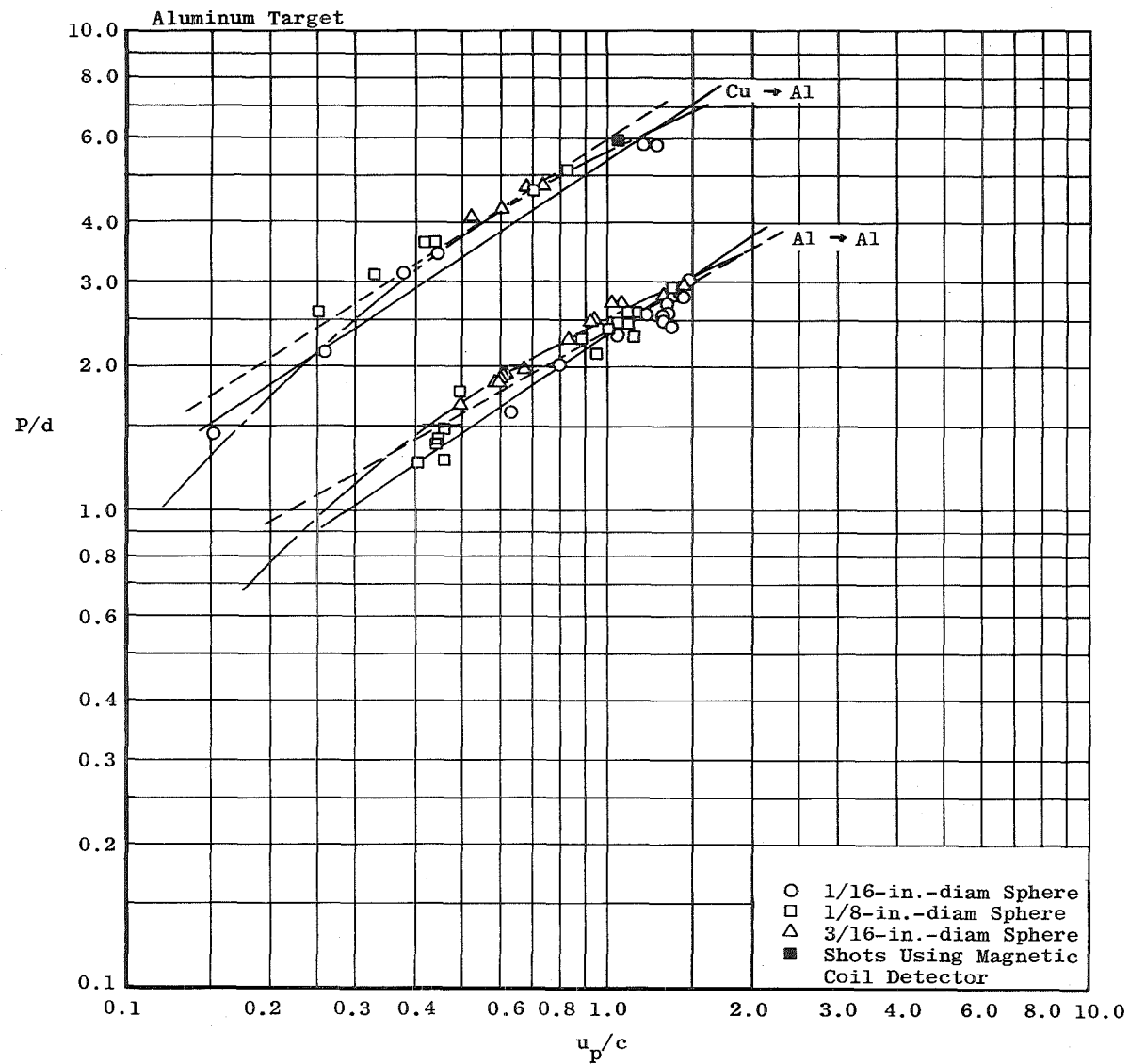


Fig. 9 Concluded

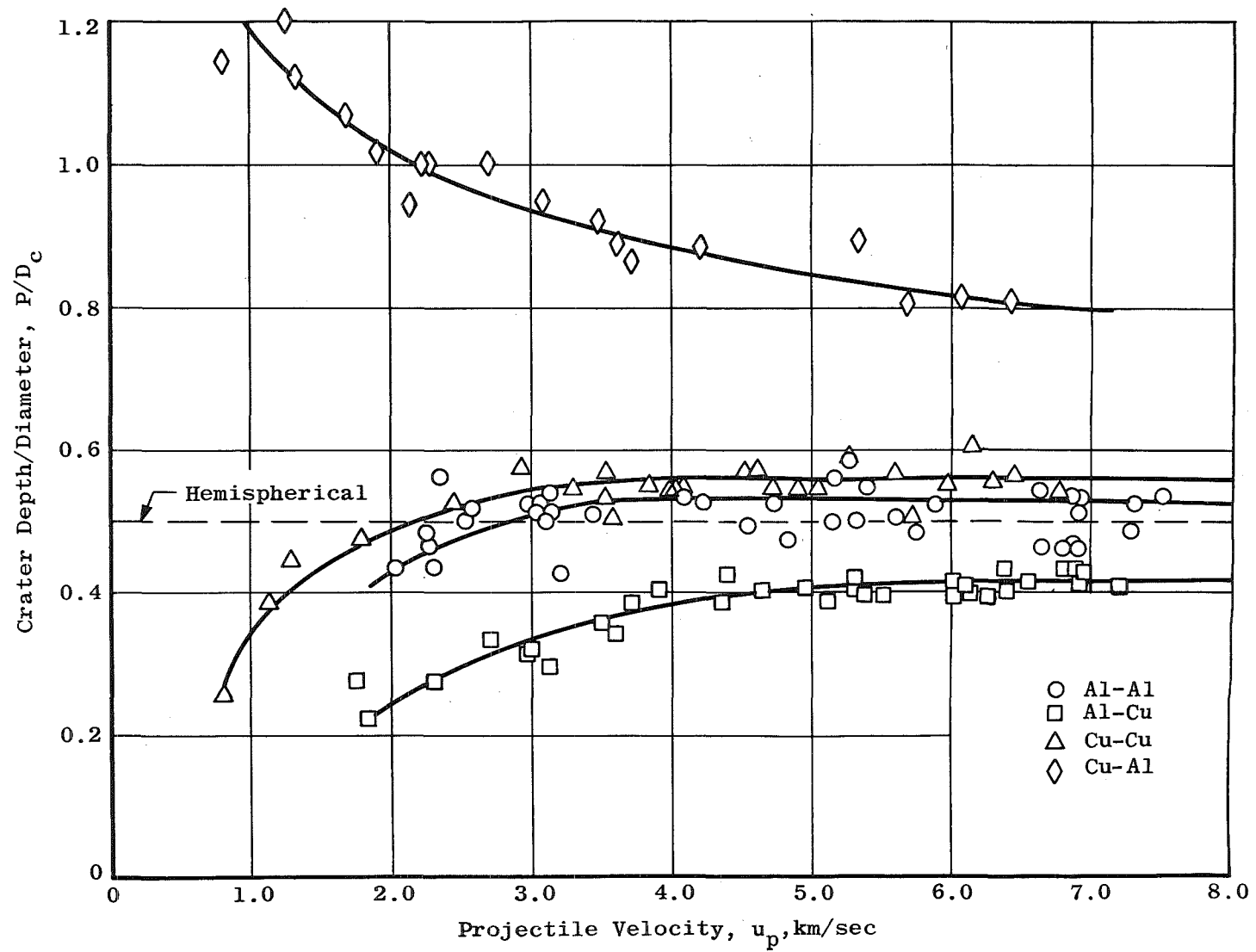


Fig. 10 Crater Depth to Diameter Ratio for Copper and Aluminum Spheres into Copper and Aluminum Targets

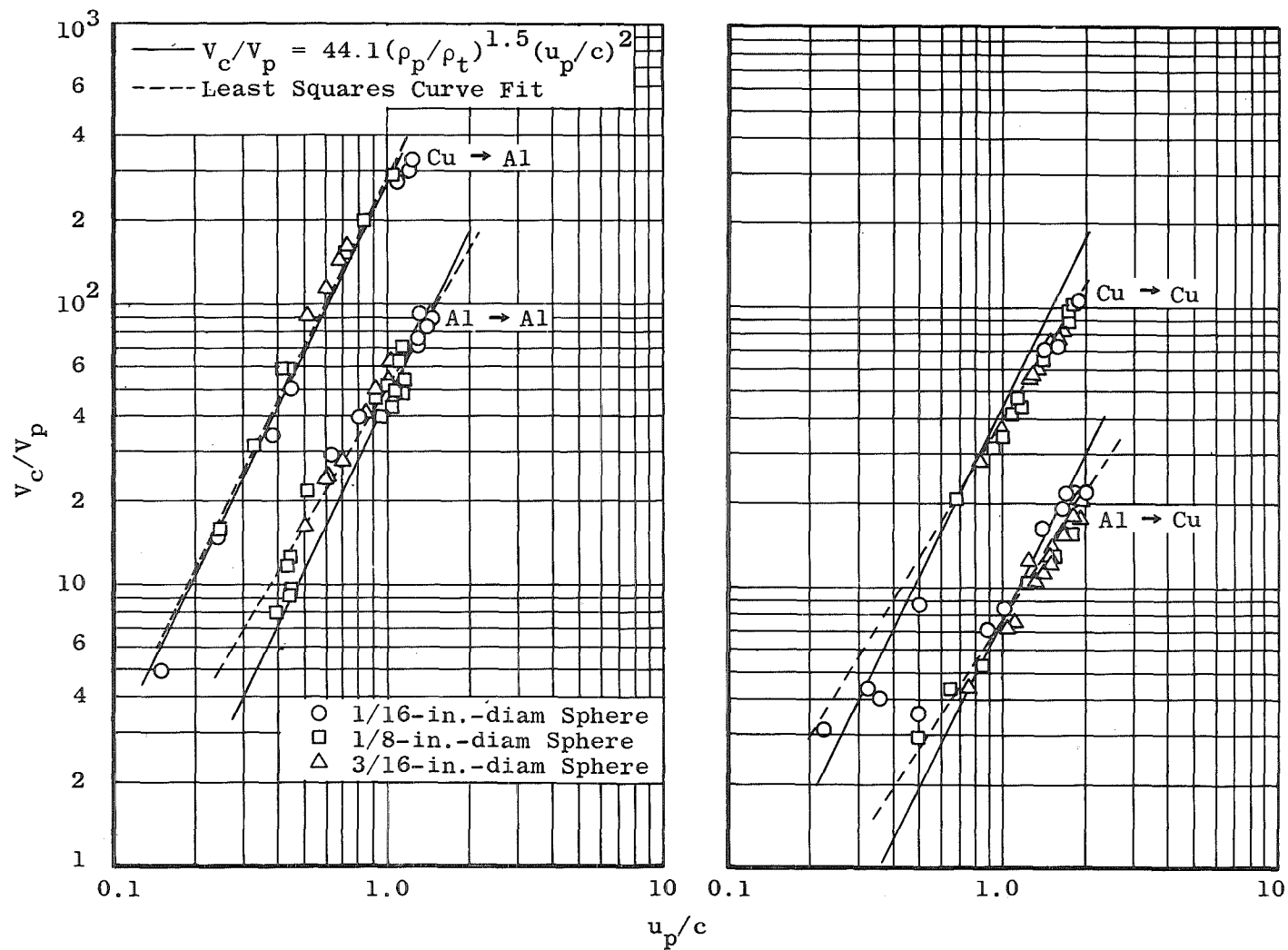


Fig. 11 Correlation of Crater Volume Data with Empirical Volume Prediction Equations

10

11

12

13

14

15

16

17

18

19

20

21

22

23

24